



High-Temperature Oxidation of NiAlCr–Ca and NiAlCr–Sr Alloys in Air

Yunus Azakli^{1,2} · Kerem Ozgur Gunduz² · Sezgin Cengiz² · Yucel Gencer² · Mehmet Tarakci²

Received: 21 September 2020 / Revised: 1 December 2020 / Accepted: 3 December 2020 /
Published online: 28 December 2020
© The Author(s) 2020

Abstract

In this study, interrupted oxidation behavior of synthetic NiAlCr–Ca (Ca=0.3, 1.4, 2 at.%) and NiAlCr–Sr (Sr=0.4 at.%) alloys in the air at 1027 °C for 192 h was investigated. Parabolic rate constants (k_p) showed that the Sr-containing alloy exhibited the best oxidation resistance among the alloys investigated in this study. The oxide scale formed on the Sr-containing alloy was composed of α -Al₂O₃ phase with Sr-rich nodules. Increasing the Ca concentration in the alloys was found to reduce the oxidation resistance due to the formation of non-protective Ca-rich complex oxides and consumption of α -Al₂O₃ scale by the reaction between Al₂O₃ and CaO. The Ca-rich complex oxides were initially formed on the Ca-rich interdendritic region and grew with time. Very little scale spallation was observed for the Sr-containing alloy, while it was notable for 0.3 at.% Ca-containing alloy. Spallation was attributed to the coefficient of thermal expansion (CTE) mismatch arisen from the formation of CaAl₄O₇ phase, a compound with a very low CTE.

Keywords NiAlCr · Calcium · Strontium · Scale spallation · High-temperature oxidation

Supplementary information The online version of this article (<https://doi.org/10.1007/s11085-020-10018-3>) contains supplementary material, which is available to authorized users.

✉ Yunus Azakli
y.azakli@sheffield.ac.uk; yunusazakli@gmail.com

¹ The Henry Royce Institute and Department of Materials Science and Engineering, The University of Sheffield, Sheffield S1 3JD, United Kingdom

² Department of Materials Science and Engineering, Gebze Technical University, 41400 Kocaeli, Turkey

Introduction

One of the reasons for material failure and high maintenance costs in the industry is the high-temperature oxidation of metallic materials under service conditions. Therefore, high oxidation resistance is a desired property along with high mechanical strength and creep resistance for the materials designed for most of the high-temperature applications [1, 2]. High-temperature oxidation resistance of metallic materials can be improved by a few methods such as alloying with Al [3] and Cr [4], applying a thermal barrier coating (TBC) [5, 6], and oxidation-resistant metallic coatings [7, 8]. TBC works as a barrier layer that reduces the heat flow rate, while metallic coatings are designed to work as a bond coat for TBC's [9] that forms protective thermally grown oxides (TGO) as in the case of alloying, such as alumina ($\alpha\text{-Al}_2\text{O}_3$) [10] or chromia (Cr_2O_3) [11]. TGO scales are desired to be dense, slow-growing, compatible with the alloy, well-adhered, free of stress, free of defects such as pores and cracks, composed of a compound with low ionic conductivity, and stable. Stress formation, especially under cyclic oxidation conditions cause spallation of TGO, which depletes the Al and Cr reservoir of the alloy or the coating. When the concentrations of Al and Cr fall below a critical level, protective oxides can no longer be maintained on the surface. Several studies have been reported which dealt with the growth and spallation mechanisms of oxide scales and ways to improve the high-temperature oxidation resistance of alloys [12, 13]. Minor addition of reactive elements (RE) such as Y, Hf [14], La [15], and Ho [16] has been reported as beneficial. The effects of RE addition include the facilitation of the scale nucleation, alteration of the scale growth mechanism by inhibiting the cation diffusion, allowing oxygen diffusion, and forming oxide pegs [17, 18], which are usually believed to increase scale adhesion. Another beneficial effect of RE addition is the inhibition of sulfur's adverse effects on the alloy properties. Sulfur as an impurity element, which is most likely introduced into Ni-base alloys with Ni element, degrades the oxidation resistance severely at elevated temperatures by reducing the bonding of alumina or chromia scale [19]. RE elements scavenge S from the molten alloy during the production stage, thus diminishing the detrimental effect of S [20]. Another well-known way to obstruct sulfur's detrimental effect is its removal by the addition of Ca, CaO, and CaF_2 into the melt to form refractory CaS inclusions [21, 22]. Afterward, formed CaS inclusions in molten metal can be eliminated by filtering during the casting. However, excess Ca dissolved in molten metal can form brittle and moisture-sensitive intermetallics with Ni; therefore, the concentration of Ca must be well-controlled for the sake of mechanical properties of the high-temperature alloys [23]. However, the influence of Ca as an impurity on the oxidation behavior of high-temperature alloys is not clear.

The influence of CaO and some Ca compounds depositions on the high-temperature degradation behavior of alloys have been studied by a few researchers. Chiang et al. [24] investigated the influence of some oxide and sulfate deposits on the oxidation behavior of NiCr, NiAl, NiCrAl, and CoCrAl. They reported that the CaO deposition increased the degradation rate of Cr_2O_3 forming alloys

and resulted in catastrophic corrosion at temperatures above 1000 °C. In addition, CaO deposition was reported to have increased the oxidation rate of alumina-forming alloys, particularly in the presence of Cr in the alloy. In a recent comprehensive study, Gheno et al. [25] investigated the reaction of CaO deposits on alumina-forming β -NiAl and NiCoCrAlY in dry air. They reported that the formation of liquid Ca–Cr–O phase at 1100 °C enhanced the diffusion of charged species. Also, alumina layer thinned down due to its consumption through the CaO–Al₂O₃ reaction; therefore, the oxidation rate was higher for CaO-deposited alloys than the deposit-free alloys.

These findings in the literature clearly show that the effect of Ca on the oxidation behavior of Ni-based alloys, especially for the alumina formers, is critical and needs more attention when it is present in the alloy as an impurity. For this purpose, in this study, interrupted oxidation behavior of three NiAlCr–Ca alloys in air at 1027 °C was investigated. In addition, due to the similarities between Ca and Sr, one Sr-containing alloy was also tested. This study is also the first report on the oxidation behavior of a Sr-containing NiAlCr alloy.

Experimental Procedures

Three NiAlCr–Ca and one NiAlCr–Sr alloys were produced from 99.9% Ni, 99.97 Al, 99.5% Cr, 99.5% Ca elements, and Al–10 Sr master alloy by melting in an atmosphere-controlled induction furnace. The molten alloys were cast into a mold made of stainless steel walls and a copper bottom plate with a 60 mm × 30 mm footprint.

The cast alloys were heat-treated in order to obtain homogenous microstructures. The samples were encapsulated in quartz ampulla before heat treatment to minimize the oxidation. The heat treatment was carried out by heating the samples at 1050 °C for 96 h, furnace-cooling to 500 °C and air-cooling to room temperature.

The designation of the alloys and the chemical compositions obtained by SEM–EDS analysis is given in Table 1. A low-speed saw with a diamond cutting wheel was utilized to section the annealed alloys into the samples with the dimensions of 14 mm × 7 mm × 2.5 mm. Absolute ethanol was used as a coolant while sectioning, grinding, and polishing the alloys to avoid Ca and Sr-rich phases dissolve in water. Microstructural examination of the alloys was conducted on both ground (180–2500 grid) and attack-polished (1 g FeCl₃:200 cc ethanol) samples since Ca and Sr-rich regions tend to dissolve during polishing. All faces of the samples to be

Table 1 Designations and chemical compositions (SEM–EDS) of the annealed alloys

Sample	Element (at.%)				
	Ni	Al	Cr	Ca	Sr
C1-A	61.1	23.7	14.9	0.3	–
C2-A	59.4	24.0	15.2	1.4	–
C4-A	55.1	27.9	15.0	2.0	–
S1-A	58.7	25.8	15.1	–	0.4

oxidized were ground using 180–1200 grid emery papers and rinsed with ethanol. The exact surface area of each sample was determined from high-resolution optical scanner images using the ImageJ software [26].

Before starting the oxidation tests, each sample and each alumina boat (oven-dried) belonging to a sample were weighed individually using a microbalance (Sartorius CPA 224S) with a 0.01 mg precision. Afterward, the boats containing samples were placed in a horizontal furnace preheated to 1027 ± 5 °C. NiAlCr–Ca and NiAlCr–Sr alloys were oxidized for a total duration of 192 h under the airflow of 90 l/h [27]. The oxidation process was carried out discontinuously in two steps: (1) 16 cycles \times 6 h/cycle and (2) 4 cycles \times 24 h/cycle. Since the weight measurement of the alloys after each interruption was carried out manually, the period of each cycle was changed from 6 to 24 h to save time after the observation of the kinetics slowing down. The previous trials showed that if an alumina boat was immediately removed from a furnace at temperatures above 1000 °C, it tended to crack due to thermal shock. A potential failure of the boat could have resulted in the spilling of the samples and the collected spall; therefore, the boat was pulled to the furnace edge and kept there until it cooled down to 800 °C to avoid due to thermal shock damage. Once the temperature reached to 800 °C, the boat was taken out to cool in the air. The temperature of the boat was measured using a pyrometer before removal. The same microbalance was used to determine the discontinuous mass gain of the samples. A Bruker D8 diffractometer (Cu $K\alpha$ at 40 kV) was employed to identify phases of the bare alloys and the oxidized samples, over a 2θ range of 10–100 with the scanning rate of 1°/min and 0.02° step size. Microstructural and chemical examinations of the annealed alloys before and after the oxidation were carried out using a Philips XL30 FEG scanning electron microscope (SEM) equipped with an energy-dispersive spectrometer (EDS). Volume fractions of phases in the alloys prior to oxidation were determined by ImageJ software on the SEM images. Plan-view examination of the oxidized samples was conducted without gold-deposition. In order to prevent charging, oxide scale on one of the edge of the sample was removed, and the sample holder and bare sample surface were interconnected using a conductive silver paste. Then, one-half of each sample was sectioned with low-speed saw, mounted in epoxy resin, ground (180–2500 grid), and attack-polished (1 g FeCl₃:200 cc ethanol) for cross-sectional examination.

Results

Microstructure of the Alloys

The SEM micrographs of annealed NiAlCr–Ca and NiAlCr–Sr alloys are given in Fig. 1. The images show that the alloys consisted of dendritic and interdendritic regions [28]. The dendritic region was composed of β -NiAl phase that contains nearly spherical α -Cr precipitates, while the interdendritic region contained γ -Ni solid solution (marked as Al_{0.9}Ni_{4.22} in XRD results), γ' -Ni₃Al, α -Cr precipitates, and Ca or Sr-rich regions. Since the solubility of Ca [29] and Sr [30] is very low in Ni, they segregated in the interdendritic region, which solidified the last. The α -Cr

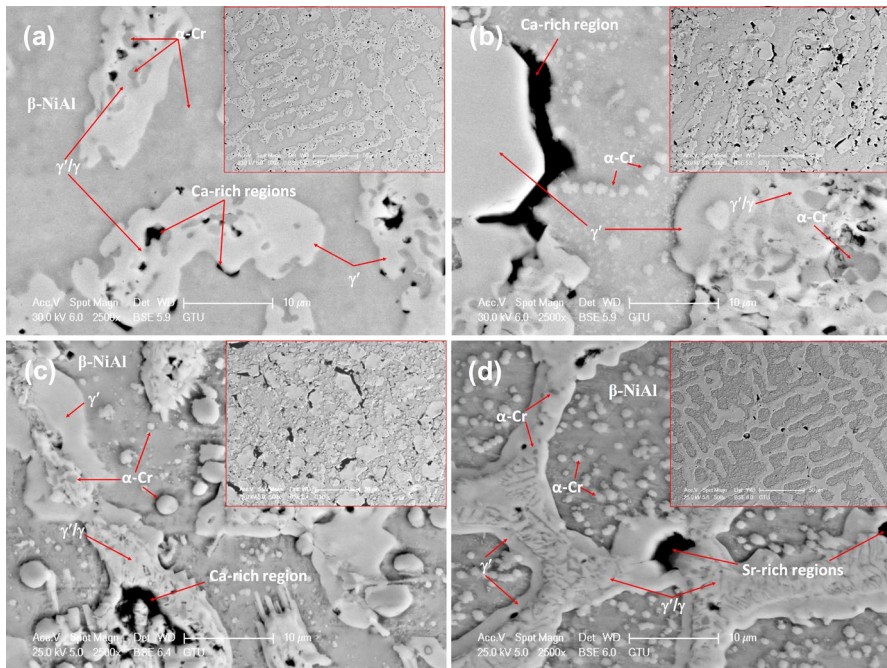


Fig. 1 SEM micrographs of annealed NiAlCr–Ca and NiAlCr–Sr alloys: **a** C1-A, **b** C2-A, **c** C4-A, and **d** S1-A

precipitates in the interdendritic region of Ca and Sr-containing alloys were coarser compared to that of Ni–27Al–14Cr (at.%) ternary alloy [31]. Volume fractions of the dendritic and interdendritic regions in the alloys and the chemical composition of various phases in these regions are given in Table 2. The EM–EDS examinations showed that the amount of Ca/Sr in β , γ , γ' and α -Cr phases was lower than 0.5 at.%. Most of the Ca and Sr in the alloy segregated in the interdendritic region. Furthermore, since Sr is very sensitive to humidity, Sr-rich regions degraded shortly after exposure to the atmosphere. Therefore, a high amount of O was detected in the Sr-rich regions. The amount of O in the region is given in round brackets next to that of Sr.

Oxidation Kinetics of the Alloys

The mass gain and mass change curves of NiAlCr–Ca (Ca=0.3, 1.4, 2) and NiAlCr–Sr (Sr=0.4) alloys oxidized at 1027 °C for 192 h in air are given in Fig. 2a, b. Zoomed in sections of the graphs were embedded in the figures for a detailed understanding of the oxidation kinetics. In order to reveal the effect of Ca and Sr further, the mass gain data of ternary Ni–27Al–14Cr alloy (M0-A), obtained under the same exposure conditions, are included in Fig. 2 as M0-A alloy [27].

Table 2 Volume fractions of the dendritic and the interdendritic regions of the annealed alloys and point SEM–EDS analysis results of various phases in the annealed alloys (O amount in the Sr-rich region is given in round brackets next to that of Sr)

Sample	Region	Volume	Phase	Element (at.%)				
				Ni	Al	Cr	Ca	Sr
C1-A	Dendritic	57.3	β	60.8	31.3	7.7	0.1	–
	Interdendritic	42.7	γ'	66.8	24.4	8.7	0.2	–
			γ'/γ	63.4	19.0	17.4	0.2	–
			α -Cr	9.2	1.5	89.1	0.2	–
C2-A	Dendritic	52.5	β	57.7	30.8	11.3	0.1	–
	Interdendritic	47.5	γ'	66.5	24.8	8.3	0.4	–
			γ'/γ	63.3	19.0	17.5	0.2	–
			α -Cr	2.7	0.1	97.0	0.2	–
Ca-rich			19.0	1.2	43.7	36.1	–	
C4-A	Dendritic	50.1	β	55.5	36.3	8.2	0.1	–
	Interdendritic	49.9	α -Cr	6.1	0.5	93.3	0.2	–
			γ'	65.7	23.3	10.4	0.7	–
			γ'/γ	64.6	15.5	19.4	0.4	–
S1-A	Dendritic	62.5	β	58.1	35.8	6.0	–	0.1
	Interdendritic	37.5	γ'	69.6	24.3	5.7	–	0.4
			γ'/γ	60.9	12.7	25.8	–	0.7
			Sr-rich	12.7	19.3	5.5	–	22.9 (O: 39.6)

The oxidation behavior of the M0-A, C2-A was parabolic, while that of S1-A and C1-A were nearly parabolic (Fig. 2a) between 0 and 192 h. The mass gain curve of C4-A approached parabolic behavior between 6 and 192 h. The mass gain data of the alloys indicated that the bare alloy surfaces oxidized rapidly in the first 6 h. The initial mass gain of the M0-A, S1-A, C1-A, C2-A and C4-A alloys were 0.34 mg/cm², 0.36 mg/cm², 0.48 mg/cm², 0.78 mg/cm² and 9.13 mg/cm², respectively. Results showed that the initial oxidation rate of the alloys was barely affected by Sr addition. However, the addition of Ca increased the initial oxidation rate, especially for C4-A alloy. After the initial stage, a notable decrease in the oxidation rate was observed for all alloys, which remained almost constant until the end of the oxidation test.

Mass change curves showed that the alloys tested in this study exhibited a positive mass change throughout the oxidation test. However, a negative trend in the mass change was reported for M0-A alloy after 12 h [27]. Moreover, the slope of C1-A alloy became negative after 96 h indicating the spallation of oxide scale.

The parabolic rate constants (k_p) calculated from the square of mass gain versus time curves are given in Fig. 2c. The relevant data and the k_p value for the M0-A alloy were also included in the figure for comparison [27]. The k_p values showed that the oxidation rate of S1-A is the lowest among all alloys presented in Fig. 2c. In addition, the oxidation rate of the alloys increased with further Ca addition. To be more precise, the oxidation rate increased approximately 170 times, with the increase in the Ca amount from 0.3 to 2 at.%. Nevertheless, the oxidation rate of

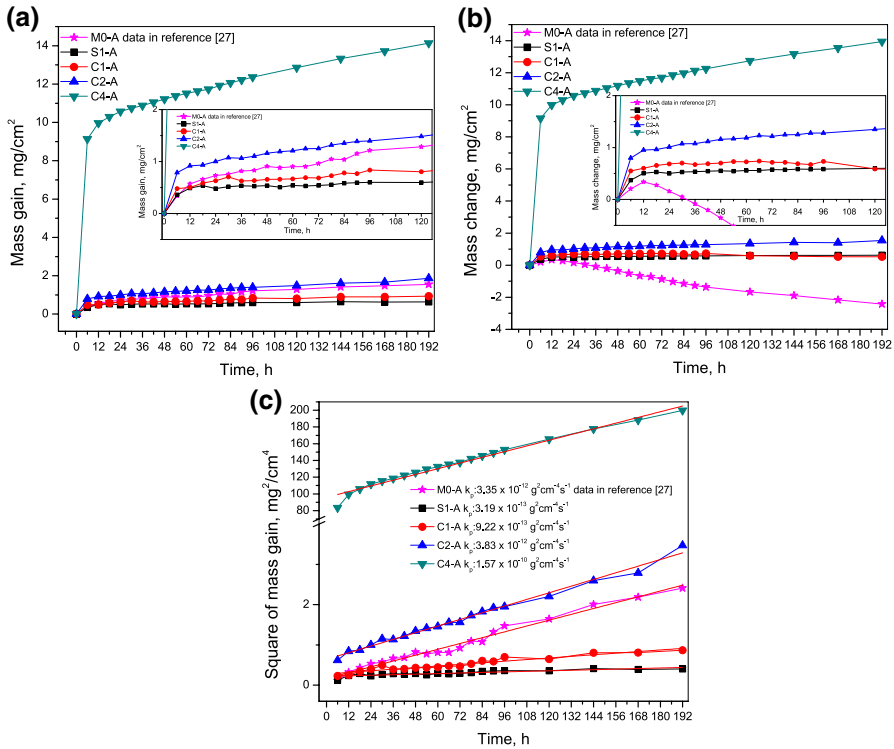


Fig. 2 Oxidation kinetics of the NiAlCr–Ca and NiAlCr–Sr alloys interruptedly oxidized at 1027 °C: **a** mass gain-time curves, **b** mass change-time curves, **c** square of mass gain-time curves (k_p values are given the legend)

M0-A was still lower than that of M2-A and M4-A alloys, although it suffered from severe spallation.

Phase Evolution of the Alloys During Oxidation

Figure 3 shows the XRD diffractograms of alloys before and after oxidation for 6, 48, 96, and 192 h. The findings are also tabulated in Table 3. The reference numbers for the phases are given in Supplemental Table S1. The unidentified peaks were marked with “x”. According to diffractograms, bare C1-A alloy consisted of β (NiAl) and γ' (Ni₃Al) intermetallic phases as well as γ (Al_{10.9}Ni_{4.22}) and α -Cr solid solutions. After 6-h oxidation, α -Cr phase vanished, while α -Al₂O₃ (will be expressed as Al₂O₃) and CaAl₄O₇ (grossite) phases appeared in the diffractogram. The intensity of the peaks belonging to Al₂O₃ increased slightly with oxidation duration, whereas that of CaAl₄O₇ did not change significantly until the end of the oxidation test. In addition, Ca₆Al₄Cr₂O₁₅ peaks were determined after 96-h oxidation. The phases identified on C2-A alloy prior to oxidation were identical to C1-A. However, on C2-A alloy, the intensity of the peaks belonging to the β -NiAl and α -Cr phases

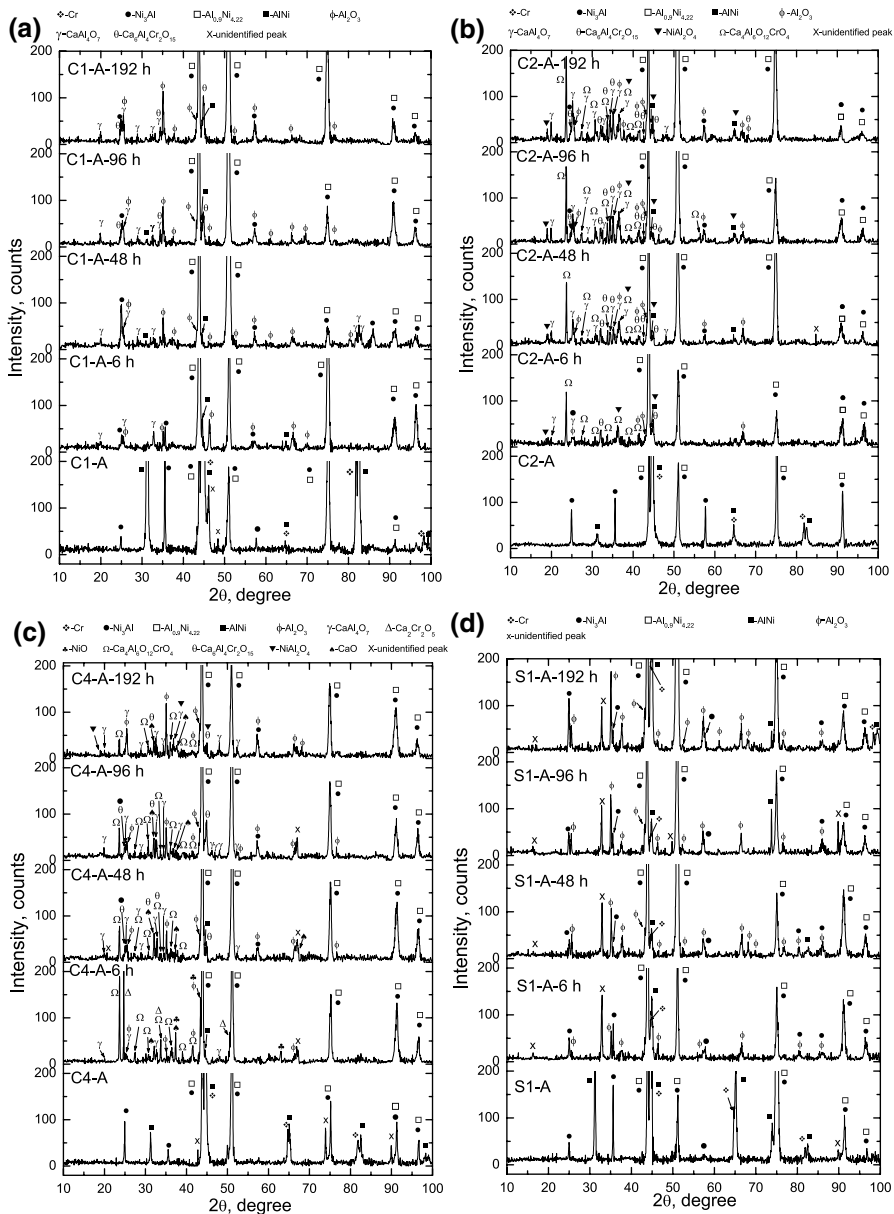


Fig. 3 XRD diffractograms of the annealed (prior to oxidation) and oxidized alloys NiAlCr–Ca and NiAlCr–Sr alloys for 6, 48, 96, and 192 h at 1027 °C: **a** C1-A, **b** C2-A, **c** C4-A, and **d** S1-A

diminished even after 6 h and completely vanished after 48 h. In addition, Al and Ca-rich $\text{Ca}_6\text{Al}_4\text{Cr}_2\text{O}_{15}$ and $\text{Ca}_4\text{Al}_6\text{O}_{12}\text{CrO}_4$ complex oxides, and NiAl_2O_4 , Al_2O_3 , and CaAl_4O_7 phases were determined following 6-h oxidation. The peaks belonging to $\text{Ca}_6\text{Al}_4\text{Cr}_2\text{O}_{15}$ and $\text{Ca}_4\text{Al}_6\text{O}_{12}\text{CrO}_4$ intensified with increasing oxidation time.

Table 3 Phases determined on the S1-A, C1-A, C2-A, and C4-A alloys before and after 6-h, 48-h, 96-h, and 192-h oxidation

Annealed state	Oxidation time			
	6 h	48 h	96 h	192 h
C1-A β -NiAl, γ' -Ni ₃ Al, γ -Ni, α -Cr; unidentified peaks	β -NiAl, γ' -Ni ₃ Al, γ -Ni, α -Al ₂ O ₃ , CaAl ₄ O ₇	β -NiAl, γ' -Ni ₃ Al, γ -Ni, α -Al ₂ O ₃ , CaAl ₄ O ₇	β -NiAl, γ' -Ni ₃ Al, γ -Ni, α -Al ₂ O ₃ , CaAl ₄ O ₇ , C ₃₆ Al ₄ Cr ₂ O ₁₅	β -NiAl, γ' -Ni ₃ Al, γ -Ni, α -Al ₂ O ₃ , CaAl ₄ O ₇ , C ₃₆ Al ₄ Cr ₂ O ₁₅
C2-A β -NiAl, γ' -Ni ₃ Al, γ -Ni, α -Cr	β -NiAl, γ' -Ni ₃ Al, γ -Ni, α -Al ₂ O ₃ , CaAl ₄ O ₇ , Ni(Al, Cr) ₂ O ₄ , Ca ₄ Al ₆ O ₁₂ CrO ₄ , C ₃₆ Al ₄ Cr ₂ O ₁₅	β -NiAl, γ' -Ni ₃ Al, γ -Ni, α -Al ₂ O ₃ , CaAl ₄ O ₇ , Ni(Al, Cr) ₂ O ₄ , Ca ₄ Al ₆ O ₁₂ CrO ₄ , C ₃₆ Al ₄ Cr ₂ O ₁₅ , unidentified peak	β -NiAl, γ' -Ni ₃ Al, γ -Ni, α -Al ₂ O ₃ , CaAl ₄ O ₇ , Ni(Al, Cr) ₂ O ₄ , Ca ₄ Al ₆ O ₁₂ CrO ₄ , C ₃₆ Al ₄ Cr ₂ O ₁₅	β -NiAl, γ' -Ni ₃ Al, γ -Ni, α -Al ₂ O ₃ , CaAl ₄ O ₇ , Ni(Al, Cr) ₂ O ₄ , Ca ₄ Al ₆ O ₁₂ CrO ₄ , C ₃₆ Al ₄ Cr ₂ O ₁₅
C4-A β -NiAl, γ' -Ni ₃ Al, γ -Ni, α -Cr; unidentified peaks	β -NiAl, γ' -Ni ₃ Al, γ -Ni, α -Al ₂ O ₃ , CaAl ₄ O ₇ , Ca ₂ Cr ₂ O ₅ , Ca ₄ Al ₆ O ₁₂ CrO ₄ , NiO, CaO, unidentified peak	β -NiAl, γ' -Ni ₃ Al, γ -Ni, α -Al ₂ O ₃ , CaAl ₄ O ₇ , Ca ₄ Al ₆ O ₁₂ CrO ₄ , C ₃₆ Al ₄ Cr ₂ O ₁₅ , CaO, unidentified peaks	γ' -Ni ₃ Al, γ -Ni, α -Al ₂ O ₃ , CaAl ₄ O ₇ , Ca ₄ Al ₆ O ₁₂ CrO ₄ , C ₃₆ Al ₄ Cr ₂ O ₁₅ , CaO, unidentified peak	γ' -Ni ₃ Al, γ -Ni, α -Al ₂ O ₃ , CaAl ₄ O ₇ , Ca ₄ Al ₆ O ₁₂ CrO ₄ , C ₃₆ Al ₄ Cr ₂ O ₁₅ , CaO, Ni(Al, Cr) ₂ O ₄
S1-A β -NiAl, γ' -Ni ₃ Al, γ -Ni, α -Cr; unidentified peak	β -NiAl, γ' -Ni ₃ Al, γ -Ni, α -Cr, α -Al ₂ O ₃ , unidentified peaks	β -NiAl, γ' -Ni ₃ Al, γ -Ni, α -Cr, α -Al ₂ O ₃ , unidentified peaks	β -NiAl, γ' -Ni ₃ Al, γ -Ni, α -Cr, α -Al ₂ O ₃ , unidentified peaks	β -NiAl, γ' -Ni ₃ Al, γ -Ni, α -Cr, α -Al ₂ O ₃ , unidentified peaks

XRD patterns of C4-A alloy obtained before and after particular periods of oxidation are given in Fig. 3c. Three unidentified peaks at 43° , 74° , and 90° were evident in the XRD pattern of C4-A alloy prior to oxidation, along with the peaks belonging to β , γ' , γ , and α -Cr phases. Formation of Al_2O_3 , CaAl_4O_7 , $\text{Ca}_2\text{Cr}_2\text{O}_5$, $\text{Ca}_4\text{Al}_6\text{O}_{12}\text{CrO}_4$, NiO , and CaO phases after 6-h oxidation was confirmed through the XRD analysis. However, the diffraction peaks of NiO vanished later, and $\text{Ca}_2\text{Cr}_2\text{O}_5$ was replaced by $\text{Ca}_6\text{Al}_4\text{Cr}_2\text{O}_{15}$ phase after 48 h.

The XRD patterns of S1-A alloy before and following particular interruption periods are given in Fig. 3d. β and γ' intermetallic phases, γ -Ni ($\text{Al}_{0.9}\text{Ni}_{4.22}$), and α -Cr solid solutions were determined on the S1-A alloy before oxidation similar to the Ca-containing alloys. A compound of Sr was not determined either before or after the high-temperature exposure. The XRD pattern of S1-A alloy prior to oxidation exhibited an unidentified peak at 90° while two more appeared at 16° and 33° after oxidation. The only oxide phase determined on S1-A alloy was Al_2O_3 . Also, the intensity of the unidentified peaks decreased with increasing exposure time, similar to that of metallic phases.

Microstructural Examination of the Oxide Scales

Figure 4 shows the plan-view SEM micrographs of C1-A, C2-A, and C4-A alloys exposed for 6 h and 192 h, and plan-view SEM–EDS maps of the C4-A alloy exposed for 192 h. In addition, SEM–EDS analysis performed on specific points was marked in the figures and their respective results are given in Table 4.

The fingerprint of the dendritic alloy microstructure was evident for C1-A alloy after 6 h (Fig. 4a). The outermost part of the oxide scale exhibited a whisker-like morphology with uneven size distribution. The region with coarse whiskers contained a lower amount of Ca (Spot A) compared to fine whiskers (Spot B), according to the SEM–EDS analysis. The mass change data of C1-A alloy showed that the alloy was prone to scale spallation after 96 h. Indeed, the microstructural examination of the oxide scale revealed spalled regions as well as regrown-oxide. Such a regrown-oxide region is shown in Fig. 4b, marked with an intermittent line.

High-temperature oxidation did not result in a whisker-like morphology for C2-A alloy (Fig. 4c). Instead, the surface of C2-A alloy was covered with dark equiaxed and bright cubical particles. The oxide scale on C2-A alloy (Fig. 4d) was continuous after 192 h, and less spallation was observed compared to C1-A alloy. According to SEM–EDS analysis (not given for this alloy), the majority of the surface was covered with equiaxed Al and Ca-rich oxides with a low amount of Cr, whereas the bright regions were rich in Ni, Al, and Cr. In line with the XRD analysis, these bright particles were determined to be NiO and $\text{Ni}(\text{Al}, \text{Cr})_2\text{O}_4$. Furthermore, localized CaO particles were observed on the outermost part of the oxide scale.

The surface of the oxidized C4-A alloy was mainly covered with Al and Ca-rich oxides after 6 h (Fig. 4e). Furthermore, Ni, Cr and Al-rich particles were also found yet more localized compared to that of C2-A alloy. The area covered with CaO grains enlarged with increasing Ca content in the alloy and oxidation duration. Also, fine NiO particles appeared in the boundaries of CaO grains (Fig. 4f). Figure 4g

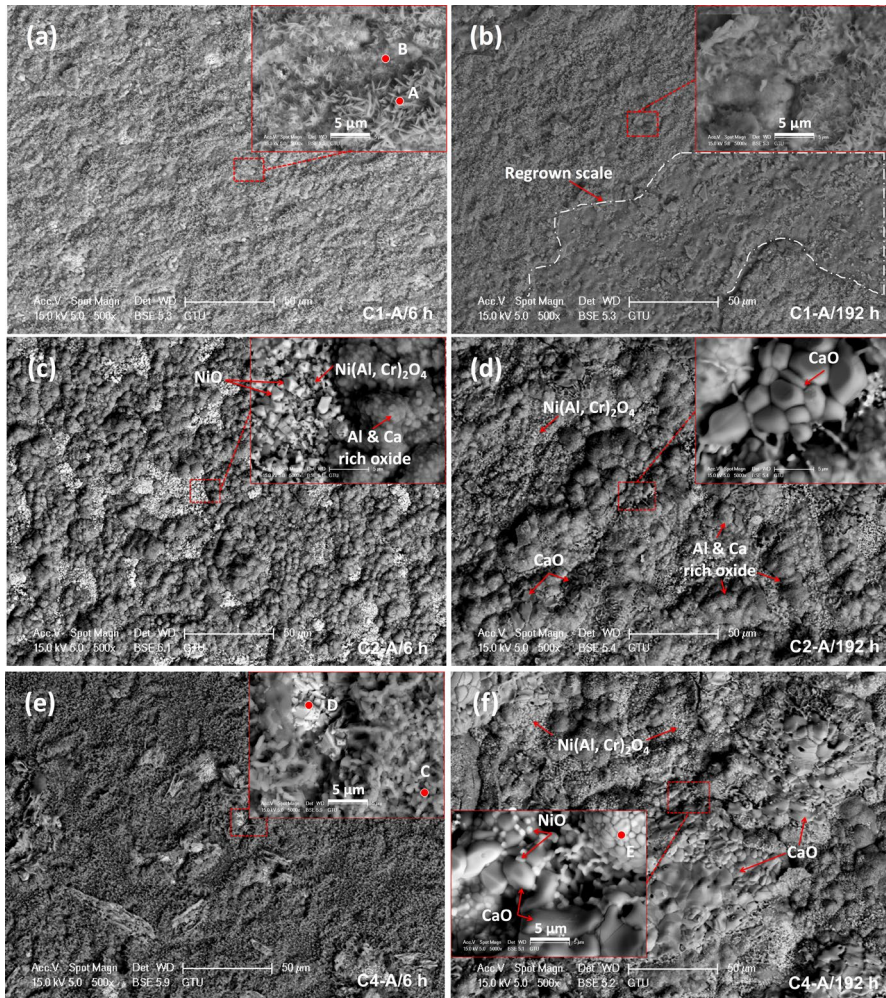


Fig. 4 Plan-view SEM images of C1-A, C2-A, and C4-A alloys after 6-h and 192-h oxidation and plan-view SEM–EDS maps of C4-A alloy after 192-h oxidation at 1027 °C: **a** C1-A 6 h, **b** C1-A 192 h, **c** C2-A 6 h, **d** C2-A 192 h, **e** C4-A 6 h, **f** C4-A 192 h, and **g** SEM–EDS maps of C4-A 192 h

shows SEM–EDS maps of the surface of C4-A alloy after 192-h oxidation. The Ca-rich regions correspond to large CaO grains while the Ni, Al, and Cr-rich regions refer to the Ni(Al, Cr)₂O₄ particles. Furthermore, the region rich in Al, Ca, and Cr is thought to be composed of CaAl₄O₇, Ca₆Al₄Cr₂O₁₅, and Ca₄Al₆O₁₂CrO₄ complex oxides.

Cross-sectional SEM micrographs of C1-A, C2-A, and C4-A alloys following the 6-h and 192-h oxidation are given in Fig. 5, and SEM–EDS results of the marked points in the figures are tabulated in Table 4. The thickness of the oxide scales after 192 h was measured as $5 \pm 2 \mu\text{m}$, $10 \pm 3 \mu\text{m}$, and $21 \pm 3 \mu\text{m}$ for C1-A,

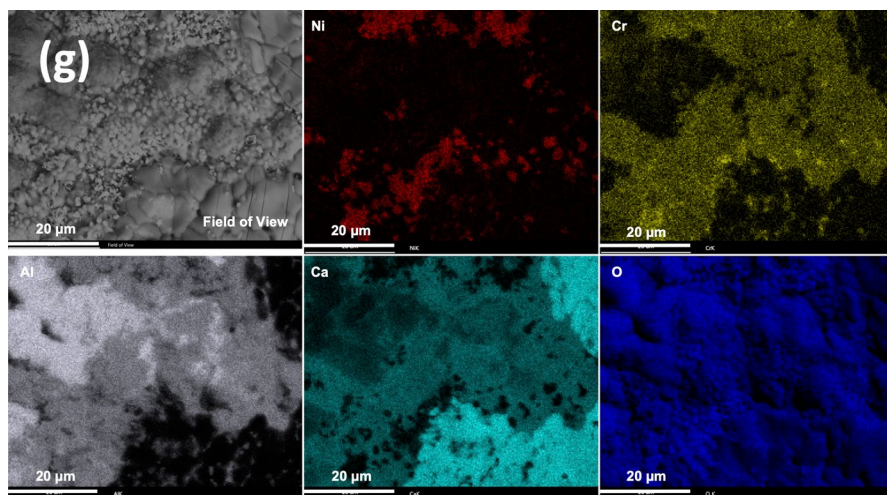


Fig. 4 (continued)

Table 4 Chemical compositions (SEM–EDS) obtained from the spots marked in Figs. 4 and 5

Figures	Spot	Element (at.%)				
		Ni	Al	Cr	Ca	O
4a	A	0.69	40.03	0.50	0.62	58.16
4a	B	0.54	34.26	0.44	6.99	57.77
4e	C	0.50	26.71	2.70	11.33	58.75
4e	D	18.91	7.28	24.33	2.07	47.41
4f	E	0.37	19.68	2.04	9.27	68.63
5a	F	1.65	54.27	1.61	1.80	40.67
5a	G	1.51	38.03	1.28	2.09	57.09
5e	H	41.64	3.42	0.73	1.15	53.07
5e	I	1.16	21.88	3.63	14.74	58.59
5e	J	5.97	36.64	2.67	2.66	52.05
5f	K	0.72	0.38	0.07	37.90	60.93
5f	L	0.90	23.47	3.96	15.50	56.17
5f	M	12.68	22.03	13.68	0.69	50.92
5f	N	0.60	40.32	0.83	4.21	54.04

C2-A, and C4-A alloys, respectively, while the thickness of the scale formed on the ternary Ni–27Al–14Cr alloy after oxidation for 192 h was measured (from the SEM image) as $5 \pm 2 \mu\text{m}$ [27]. Cross-sectional SEM examinations of the Ca-containing alloys revealed the existence of oxide intrusions in the alloy. These intrusions were concentrated on the Ca-rich regions within the alloy. Oxide intrusions were found to grow with increasing exposure time and Ca concentration in

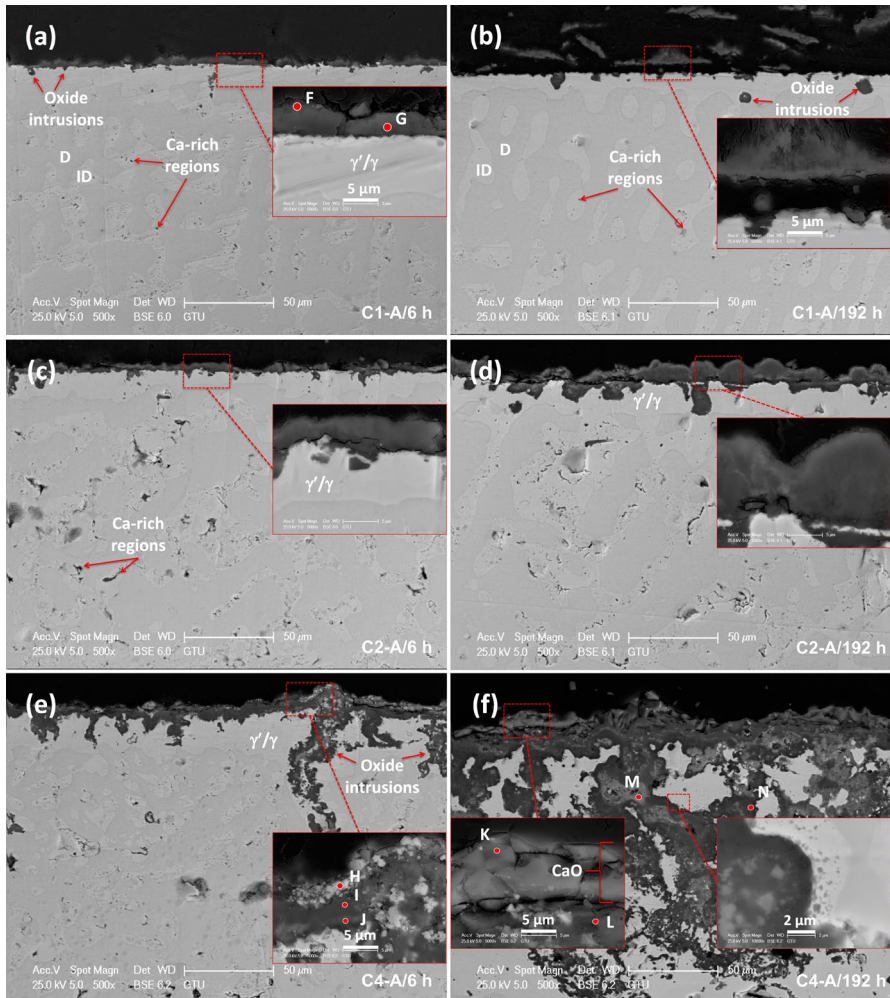


Fig. 5 Cross-sectional SEM images of C1-A, C2-A and C4-A alloys after 6-h and 192-h oxidation at 1027 °C: **a** C1-A 6 h, **b** C1-A 192 h, **c** C2-A 6 h, **d** C2-A 192 h, **e** C4-A 6 h, and **f** C4-A 192 h

the alloy. The depth of these intrusions was measured as $9 \pm 3 \mu\text{m}$, $26 \pm 9 \mu\text{m}$ and $107 \pm 31 \mu\text{m}$ for C1-A, C2-A, and C4-A alloys, respectively.

The cross-sectional SEM image of the C1-A alloy obtained after 6-h oxidation showed that the alloy region in the vicinity of the oxide/alloy interface went through a phase transformation (β -depletion) to form a continuous γ'/γ zone. Furthermore, Ca-rich regions did not exist in the newly formed γ'/γ region. The SEM–EDS results of spots F and G in Fig. 5a indicated that the scale was mainly composed of Al_2O_3 and contained a low amount of Ca, Cr, and Ni. The oxide scale on the alloy showed a tendency to spall during sectioning and

microstructural preparation. The fragments of the detached scale can be clearly seen in Fig. 5b for C1-A alloy following 192 h oxidation.

The cross-sectional SEM images of C2-A are given in Fig. 5c, d. The oxide scale and the oxide/alloy interface were undulated on this alloy. With further exposure, the thickness of the oxide scale increased and the γ/γ' region enlarged. Moreover, the oxide intrusions were larger and penetrated deeper in C2-A alloy than in C1-A.

The cross-sectional SEM images of C4-A are given in Fig. 5e, f. The oxide intrusions were found to penetrate up to 60 μm even after 6 h. The magnified image of the oxide scale in Fig. 5e revealed the existence of bright oxide particles in the oxide scale as well as near the gas/oxide interface. The large particles were determined to be NiO (Spot H) while the fine particles were $\text{Ni}(\text{Al}, \text{Cr})_2\text{O}_4$. The relatively darker, continuous region in the middle of the scale was composed of Al, Ca, Cr, and a small amount of Ni (Spot I). SEM-EDS results also revealed the presence of Ni, Al, and Cr-rich fine particles near the oxide/metal interface and within the oxide intrusions. After 192 h, the intrusions, with depths reaching up to 140 μm , covered a large volume within the alloy (Fig. 5f). A distinct and continuous CaO layer was found in the outermost part of the oxide scale. Beneath this layer, a Ca and Al-rich oxide layer with fine Ni, Al and, Cr-rich oxide particles were found.

Figure 6 shows the plan-view SEM micrographs of S1-A alloy following 6- and 192-h oxidation. The surface of the S1-A alloy was covered with a continuous oxide scale with nodules after 6 h (Fig. 6a). Also, slight spallation was observed. Whisker-like morphology was dominant on the oxide surface in addition to the regions with fine oxide grains. According to the SEM-EDS results in Table 5, both regions consisted of Al_2O_3 (Spot A and B). It should be noted that the high amount of Cr and Ni detected on Spot B might be misleading since it represents the thin section of the scale. Several nodules were found on the oxide surface with high Sr content (Spot C). The metal surface in the spalled regions had cavities with a thermally faceted appearance. Moreover, the imprints of fine Al_2O_3 grains were evident around the cavities. Even though it was slight, spallation resulted in the metal surface to expose and oxidize during the interrupted

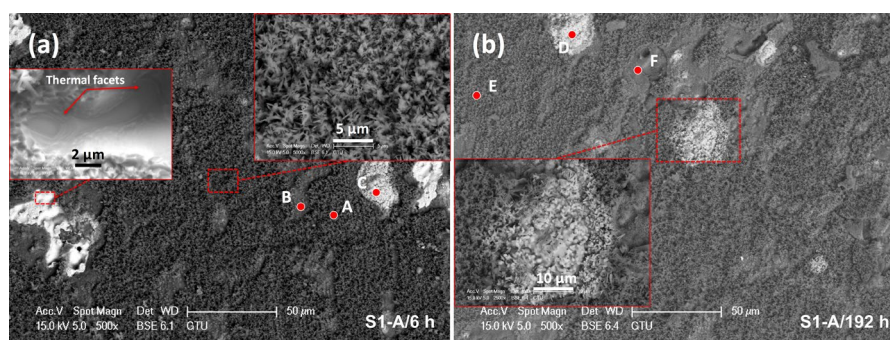


Fig. 6 Plan-view SEM images of S1-A alloy after **a** 6-h and **b** 192-h oxidation at 1027 °C

Table 5 Chemical compositions (SEM–EDS) obtained from the spots marked in Figs. 6 and 7

Figures	Spot	Element (at.%)				
		Ni	Al	Cr	Sr	O
6a	A	1.05	46.01	0.59	0	52.36
6a	B	0.80	40.76	0.69	0.32	57.43
6a	C	1.18	30.81	2.36	8.48	57.18
6b	D	1.04	30.35	2.23	8.22	58.15
6b	E	1.03	37.98	0.50	0.49	60.01
6b	F	3.32	48.66	0.75	0.18	47.08
7a	G	0.99	48.65	0.70	0.19	49.46
7a	H	62.63	15.57	21.4	0.40	–
7a	I	65.69	24.93	8.96	0.42	–
7a	J	58.88	33.41	7.38	0.34	–
7c	K	1.85	33.68	4.71	18.70	41.06
7c	L	3.34	53.77	5.42	3.29	34.17

tests. SEM–EDS analysis confirmed the formation of an Al_2O_3 scale with much finer grains on the spalled regions with further oxidation. The morphology of the surface did not change significantly until the end of the oxidation test.

Cross-sectional SEM examinations of S1-A alloy showed that a thin and continuous scale was formed during the high-temperature exposure (Fig. 7). Examinations revealed the existence of cracks in the scale and partial detachment of the scale from the alloy. These cracks were thought to have developed during sample preparation. Point SEM–EDS analysis results obtained from the marked regions are given in Table 5. These results confirmed the formation of Al_2O_3 on the alloy. Also, a low amount of Ni and Cr, and a trace amount of Sr was determined on the scale. Nevertheless, since SEM–EDS analysis is not that sensitive, it was thought that the percentage of the Sr element might also be misleading. Similar to the Ca-containing alloys, a continuous γ'/γ zone was found beneath the scale (Spot B). However,

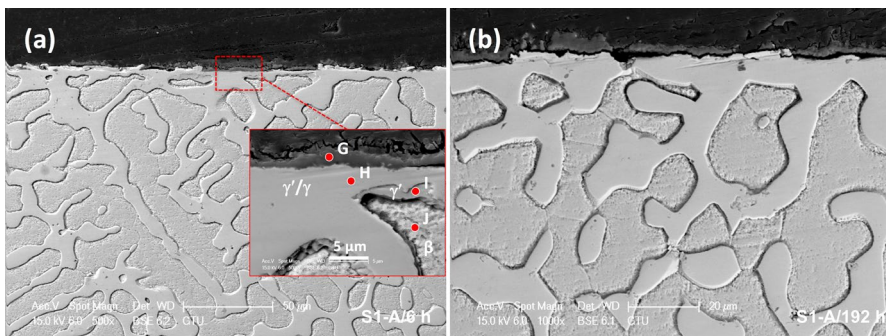


Fig. 7 Cross-sectional SEM images of S1-A alloy after **a** 6-h and **b** 192-h oxidation, and **c** cross-sectional SEM–EDS maps of S1-A alloy after 192-h oxidation at 1027 °C

the thickness of this zone was lower compared to C1-A throughout the oxidation test. γ'/γ zone enlarged in parallel with the oxide scale growth. Sr amount in the Al_2O_3 scale was very low except for the nodules formed on the top of the Sr-rich regions near the alloy surface. Figure 7c shows the cross-sectional SEM–EDS maps of such a nodule observed on S1-A alloy after 96-h oxidation. The SEM–EDS maps indicated that the nodule was composed of Al and Sr-rich oxides. The alloy region beneath the nodule was rich in oxygen, indicating the existence of a Sr-rich reserve near the alloy surface prior to oxidation.

Discussion

The interrupted oxidation behavior of NiAlCr–Ca and NiAlCr–Sr alloys at 1027 °C was investigated. The alloy with Sr had the best oxidation resistance among the alloys tested in this study, while Ca addition in the alloys reduced the oxidation resistance. Besides, only the Sr-containing alloy developed a single phase Al_2O_3 scale, while various mono-oxides and complex oxides were found on Ca-containing alloys. Thus, the oxidation and spallation resistance of the alloys were subject to the characteristics of the oxides formed on the alloy throughout the oxidation tests.

Most of the oxide products formed on the alloys were developed at the initial oxidation stage (<6 h). The oxidation rate was high at this stage since the oxide film was thin and non-protective. The standard free energy of formation of the relevant metal oxides per one mol O_2 at 1027 °C, Ca (2CaO : $\Delta G^\circ_{1300\text{K}} = -916$ kJ), Sr (2SrO : $\Delta G^\circ_{1300\text{K}} = -996$ kJ) and Al ($2/3\text{Al}_2\text{O}_3$: $\Delta G^\circ_{1300\text{K}} = -840.6$ kJ) show that these elements can form highly stable oxides [32]. Therefore, rapid preferential oxidation of particularly Al and Ca/Sr took place until a protective scale was formed.

Since both Ca and Sr were segregated in the interdendritic region as Ca/Sr-rich islands, the oxide scale formed on the Al-rich dendritic region was mainly alumina for low-alloyed S1-A and C1-A alloys. Formation of alumina was also reported by Azakli et al. [27] for ternary Ni–27Al–14Cr alloy, which was tested under the same conditions of temperature and interruption period. The surface of the oxide scale on these alloys mainly contained a whisker-like morphology. The presence of the whiskers, which is an indicator of fast outwards cation diffusion, confirmed the existence of non-protective transient alumina prior to the formation of a protective $\alpha\text{-Al}_2\text{O}_3$ scale on the alloy [33]. There are several studies on the transformation kinetics of metastable alumina to $\alpha\text{-Al}_2\text{O}_3$. It is known that the addition of Ca^{2+} , Sr^{2+} , and Be^{2+} can stabilize the transition alumina compounds [34], while Fe^{3+} , Mn^{3+} , and Cr^{3+} can facilitate their transformation to $\alpha\text{-Al}_2\text{O}_3$ [35]. The length of the whiskers formed on the dendritic region of C1-A and S1-A alloys after 6 h were measured with the aid of ImageJ software, which were determined to be 1.7 ± 0.2 μm , 1.9 ± 0.4 μm for C1-A and S1-A, respectively. The length of the whiskers formed on the dendritic region of the ternary Ni–27Al–14Cr alloy was also measured to reveal the influence of the Ca and Sr impurities on the growth of the whiskers [27]. The whiskers formed on M0-A after 192-h oxidation were measured to be $0.6 \mu\text{m} \pm 0.1$ long, nearly one-third of those formed on Ca and Sr-containing alloys. These values confirm that the transient alumina to $\alpha\text{-Al}_2\text{O}_3$ transformation takes longer time in the presence of Ca or Sr as

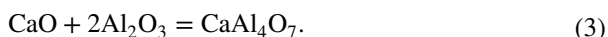
an impurity in β -NiAl phase. However, the amount of Cr in the alloy/phase region influences the transformation rate. The alloys and distinct even phases with high Cr content (third element effect) were demonstrated to develop a thin Al_2O_3 scale. The development of a thin Al_2O_3 is attributed to the formation of Cr_2O_3 with corundum structure (due to preferential oxidation), which functions as a template for α - Al_2O_3 nucleation and growth. [36]. Therefore, whisker-like morphology was not observed for the alumina scale formed on the Cr-rich interdendritic region of S1-A alloy since the rapid formation of α - Al_2O_3 slowed down the cation diffusion. The oxidation rate decreased after the development of a continuous α - Al_2O_3 layer within the scale. It should be noted that the transformation from transient to α - Al_2O_3 must have been completed before 6 h since no transient alumina phase was determined via XRD analysis.

Preferential oxidation of Al led to the depletion of the β phase and dissolution of Cr, which promoted the formation of γ'/γ zone near the oxide/alloy interface with time. Al in the S1-A alloy was consumed mainly to form Al_2O_3 phase, except for the Sr-rich nodules. However, Al_2O_3 phase reacted with CaO and other oxides to form more stable but non-protective complex oxides for Ca-rich alloys, which reduced the oxidation resistance significantly.

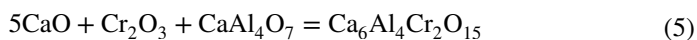
The visual inspections, SEM examinations, and mass gain-time data curves indicated that the scale spallation occurred during oxidation tests. Rapid oxide growth, phase transformations, and the discrepancy between the CTE of the phases are known to result in stress accumulation on the scale. The stress delivered by scale growth sometimes leads to the local detachment of the scale and formation of a convoluted morphology on the oxide surface [12]. In this case, oxidation proceeds through the evaporation and condensation of metal from the substrate surface to oxide scale, which results in a smooth, thermally faceted appearance on the alloy surface, as demonstrated for S1-A in Fig. 6a. A similar appearance was also reported for alumina-forming NiTaAl and FeCrAl alloys [37, 38]. C1-A exhibited the best oxidation resistance among Ca-containing alloys; however, it also suffered from spallation. This behavior is apparent in the mass change curve of C1-A alloy after 96 h (Fig. 2b), where the slope becomes negative. The ternary Ni-27Al-14Cr alloy (M0-A) reportedly established a single-phase alumina scale after 6 h; however, since the alloy suffered from continuous scale spallation, a thick NiCr_2O_4 layer was formed at the outermost part of the scale. Nevertheless, the formation of a continuous Al_2O_3 scale for M0-A alloy in the oxide/alloy interface during the oxidation period limited the oxidation rate to a reasonable value, roughly threefold higher than that of the C1-A [27]. For C1-A alloy, on the other hand, selective oxidation of Al and Ca resulted in the formation of Al_2O_3 and CaAl_4O_7 (CA_2) within 6 h. CaAl_4O_7 , which is known as grossite, is a compound with a very low CTE. The average linear CTE of this compound was reported as 1.2×10^{-6} and $4.1 \times 10^{-6} \text{ K}^{-1}$ at 100 and 900 °C, respectively [39], while the mean linear CTE of Al_2O_3 is about $8.1 \times 10^{-6} \text{ K}^{-1}$. Therefore, notable scale spallation for C1-A can be attributed to stress accumulation due to the CTE incompatibility of oxide/oxide and oxide/alloy, which becomes significant, particularly in cyclic/interrupted conditions.

Reportedly, Ca^{2+} diffusion plays a crucial role in the $\text{CaO-Al}_2\text{O}_3$ reaction, which controls the growth of calcium aluminates [40–42]. The presence of other intermediate

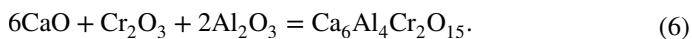
phases (CA and CA₃) in the Al₂O₃–CaO system is also possible; however, CaAl₄O₇ was the only one determined through XRD analysis among the possible phases. The proposed oxidation reactions are given as follows:



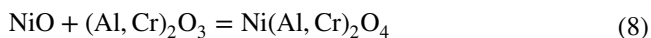
During the formation of CaAl₄O₇, Al₂O₃ layer in the scale was partially consumed, which reduced its oxidation resistance [25] and resulted in an enhanced the O²⁻ flux toward to metal. This led to the participation of Cr in the oxidation reaction to form Ca₆Al₄Cr₂O₁₅ (Cr³⁺) complex oxide. Kaiser et al. [43] reported the formation of Ca₆Al₄Cr₂O₁₅ compound with the reaction of CaO–CaCr₂O₄–CaAl₂O₄ under mildly reducing atmosphere. Similarly, Song et al. [44, 45] reported the formation of Ca₆Al₄Cr₂O₁₅ compound by the reaction of Cr₂O₃ with Ca₃Al₂O₆ and Ca₁₂Al₁₄O₃₃ in CO₂ atmosphere. The formation reactions for these compounds can be summarized as below:

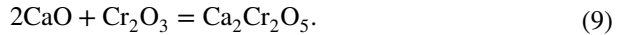


or

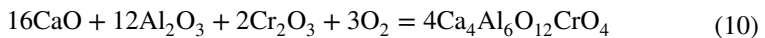


In addition to the aforementioned phases for C1-A alloy, Ni(Al, Cr)₂O₄ and Ca₄Al₆O₁₂CrO₄ (Cr⁶⁺) complex oxides developed on C2-A and C4-A during high-temperature exposure. Also, Ca₂Cr₂O₅ phase was determined following 6-h oxidation, but it disappeared later. Since C2-A and C4-A comprise more Ca compared to C1-A alloy, the amount of oxidized Ca was higher. This, in turn, led to exaggerated consumption Al₂O₃ for the formation of complex oxides, which even more enhanced the O²⁻ flux to the oxide/alloy interface and resulted in catastrophic degradation of the alloy. The degradation was so severe for C2-A and C4-A alloys that NiO particles were found in the CaO clusters on the oxide surface. It should be noted that NiO has limited solubility in CaO at the oxidation temperature and no intermediate compound forms with the reaction of these two oxides [46]. Along with its presence as monoxide, NiO reacted with (Al, Cr)₂O₃ to form Ni(Al, Cr)₂O₄ phase on the surface. The formation reactions for NiO, NiAl₂O₄, and Ca₂Cr₂O₅ [47] can be given as follows:





Vaporization of Cr from Cr_2O_3 during high-temperature exposure is a known phenomenon [48]. It was also reported that the presence of free CaO could accelerate the vaporization by favoring the formation of CrO_3 where the oxidation state of Cr is + 6 [24]. It should be noted that the formation of $\text{Ca}_4\text{Al}_6\text{O}_{12}\text{CrO}_4$ (Cr^{6+}) phase was only observed for C2-A and C4-A alloys. Therefore, it is thought that the formation of $\text{Ca}_4\text{Al}_6\text{O}_{12}\text{CrO}_4$ (Cr^{6+}) phase was facilitated by the presence of high CaO content within the scale. Equation 10 demonstrates the reaction in which Cr_2O_3 oxidizes further and changes its oxidation state to Cr^{6+} [45].



Mass gain-time curves and k_p values show that the degradation rate increases with the further addition of Ca to the alloys. The severity of degradation is related to resulting complex oxides by the reaction of the protective Al_2O_3 with CaO and with other oxides. Chiang et al. [24] investigated the degradation of CaO-deposited Al_2O_3 and Cr_2O_3 forming alloys. They found out that CaO deposits influence the degradation rate of chromia-forming alloys by two mechanisms: (1) vaporization of CrO_3 and (2) liquid calcium chromate formation on the scale. They also reported that the reaction of transient Cr_2O_3 with CaO on the surface of alumina-forming NiCrAl and CoCrAl alloys resulted in severe corrosion. Gheno et al. [25] studied the high-temperature corrosion of CaO-deposited NiCoCrAlY alloys and found that the degradation in CaO-deposited alloys were catastrophic. They concluded that the formation of liquid phase calcium chromate on the scale and the reaction between protective Al_2O_3 and CaO increased the degradation rate. In the present study, oxide intrusions were observed near the original metal surface in the early stages of oxidation. The oxide intrusions grew into the alloy through Ca-rich interdendritic region, which functioned as pathways for cation transport to surface and O^{2-} transport inwards. The fast diffusion of O^{2-} led to enhanced oxidation of Al, Cr, and Ni; thus, Al–Ca oxides and also large $\text{Ni}(\text{Al}, \text{Cr})_2\text{O}_4$ formed far beneath the oxide/alloy interface. This explains why the oxidation rate of Ca-rich alloys, particularly C4-A, was relatively higher than it was reported for CaO-deposited alloys.

Two different eutectic temperatures were reported in the literature for CaO– Cr_2O_3 system; 1022 °C [49] and 1061 °C [43]. Therefore, one might expect the formation of a liquid phase within the scale during exposure at 1027 °C that could increase the degradation rate of the alloys. Moreover, it is quite obvious that the oxidation temperature is high enough for the formation of a Ca-rich eutectic (Ca–Ni eutectic: 627 °C) within the alloy [29]. Since the activity and the diffusion rate of elements are higher in liquid phase, oxidation is expected to occur faster. Therefore, especially for C4-A, in which large Ca-rich precipitates were present in the alloy microstructure, liquid phase formation was also likely to be responsible for the abrupt increase in the oxidation rate.

Similar to Ca, Sr mainly segregated in the interdendritic region of the alloy. SEM examinations following grinding (without polishing) showed that the Sr-rich region on the surface of the alloy tended to oxidize shortly after exposure

to air at room temperature. It is known that Sr can form a eutectic with Ni at 652 °C and also the NiSr intermetallic melts at 861 °C [30]. Therefore, Sr-rich regions close to the alloy surface rapidly oxidized to form oxide nodules. The SEM–EDS results showed that the nodules were rich in Sr and Al and contained a low amount of Cr. Due to similarities between Sr and Ca, one can assume that the nodule includes oxides with the same structure of $\text{Ca}_6\text{Al}_4\text{Cr}_2\text{O}_{15}$ or $\text{Ca}_4\text{Al}_6\text{O}_{12}\text{CrO}_4$ compounds. However, there is no thermodynamic or XRD diffraction data to confirm this for the time being.

S1-A alloy exhibited better oxidation and spallation resistance than C1-A, C-A, C4-A and the ternary Ni–27Al–14Cr alloy [30] tested under the same conditions. Although Sr addition improved both the oxidation and spallation resistance of the alloy, the reason behind this effect is not known. By evaluating the beneficial effect of RE elements, one possible explanation could be that Sr scavenged the S from the alloy and in return increased the adhesion strength of the oxide scale. However, further studies are needed to verify this hypothesis.

Conclusions

The interrupted oxidation tests of three Ca-containing (0.3, 1.4 and 2 at.%) and one Sr-containing (0.4 at.%) NiAlCr alloys were carried out at 1027 °C in flowing air and the oxidation behavior of the alloys were compared with the behavior of the ternary Ni–27Al–14Cr (at.%) alloy [27] tested under the same parameters. Parabolic rate constants (k_p) were calculated using the square of mass gain-time data. The oxide scales were examined using XRD, SEM, and SEM–EDS.

- Sr-containing alloy exhibited a much better spallation resistance under cyclic conditions in comparison with the previously studied Ni–27Al–14Cr alloy [27]. Sr-containing alloy exhibited the best oxidation resistance among the alloys tested in this study. Parabolic rate constant (k_p) for S1-A was found as $3.19 \times 10^{-13} \text{ mg}^2/\text{cm}^4$, which was near one-tenth of the k_p value reported for the ternary Ni–27Al–14Cr alloy [27].
- Sr-containing alloy developed a continuous Al_2O_3 scale with Sr-rich nodules, whereas Al_2O_3 , CaAl_4O_7 , $\text{Ca}_6\text{Al}_4\text{Cr}_2\text{O}_{15}$, $\text{Ca}_4\text{Al}_6\text{O}_{12}\text{CrO}_4$, NiAl_2O_4 complex oxides, and NiO and CaO were found on Ca-containing alloys.
- Formation of $\text{Ca}_4\text{Al}_6\text{O}_{12}\text{CrO}_4$ (Cr+6) was observed only for the alloys (C2-A and C4-A) containing 1.4 and 2 at.% Ca.
- The high-temperature oxidation rate of the alloy containing 2 at.% Ca was 170 times higher than that of the alloy containing 0.3 at.% Ca.
- Oxidation of segregated Ca in the interdendritic region of the alloy resulted in the formation of oxide intrusions. These intrusions enlarged with increasing oxidation duration and Ca amount in the alloy.
- Presence of Ca/Sr impurities in the β -NiAl phase retarded the transformation of transient Al_2O_3 to α - Al_2O_3 in the initial oxidation stage, which in turn resulted in the coarsening of the whiskers on the oxide surface.

Acknowledgements The authors acknowledge the help of technicians Ahmet Nazim and Adem Sen performing the SEM and XRD examinations. One of the authors of this work, Yunus Azakli, acknowledges the financial support of Scientific and Technological Research Council of Turkey through the Program No. of TUBITAK-2211-C.

Open Access This article is licensed under a Creative Commons Attribution 4.0 International License, which permits use, sharing, adaptation, distribution and reproduction in any medium or format, as long as you give appropriate credit to the original author(s) and the source, provide a link to the Creative Commons licence, and indicate if changes were made. The images or other third party material in this article are included in the article's Creative Commons licence, unless indicated otherwise in a credit line to the material. If material is not included in the article's Creative Commons licence and your intended use is not permitted by statutory regulation or exceeds the permitted use, you will need to obtain permission directly from the copyright holder. To view a copy of this licence, visit <http://creativecommons.org/licenses/by/4.0/>.

References

1. J. B. Wahl and K. Harris, *Proceedings of the ASME Turbo Exposition* **6**, 179–188 (2014).
2. A. Sato, Y. L. Chiu and R. C. Reed, *Acta Materialia* (2011). <https://doi.org/10.1016/j.actamat.2010.09.027>.
3. R. Prescott, D. F. Mitchell and M. J. Graham, *Corrosion* **50**, 62–71 (1994).
4. H. Hindam and D. P. Whittle, *Oxidation of Metals* **18**, 245–284 (1982).
5. E. A. G. Shillington and D. R. Clarke, *Acta Materialia* (1999). [https://doi.org/10.1016/S1359-6454\(98\)00407-8](https://doi.org/10.1016/S1359-6454(98)00407-8).
6. D. R. Clarke and C. G. Levi, *Annual Review of Materials Research* (2003). <https://doi.org/10.1146/annurev.matsci.33.011403.113718>.
7. K. A. Gamble, T. Barani, D. Pizzocri, J. D. Hales, K. A. Terrani and G. Pastore, *Journal of Nuclear Materials* (2017). <https://doi.org/10.1016/j.jnucmat.2017.04.039>.
8. W. Zhong, P. A. Mouche, X. Han, B. J. Heuser, K. K. Mandapaka and G. S. Was, *Journal of Nuclear Materials* (2016). <https://doi.org/10.1016/j.jnucmat.2015.11.037>.
9. W. R. Chen, X. Wu, B. R. Marple, D. R. Nagy and P. C. Patnaik, *Surface and Coatings Technology* (2008). <https://doi.org/10.1016/j.surfcoat.2007.09.042>.
10. G. H. Meng, H. Liu, M. J. Liu, et al., *Surface and Coatings Technology* (2019). <https://doi.org/10.1016/j.surfcoat.2019.04.046>.
11. M. P. Taylor, H. E. Evans, S. Gray and J. R. Nicholls, *Materials and Corrosion* (2011). <https://doi.org/10.1002/maco.201005881>.
12. F. H. Stott and G. C. Wood, *Materials Science and Engineering* **87**, 267–274 (1987).
13. D. P. Whittle and J. Stringer, *Philosophical Transactions of the Royal Society of London. Series A, Mathematical and Physical Sciences* **295**, 309–329 (1980).
14. W. T. Chen, B. Gleeson and A. Heuer, *Oxidation of Metals* **92**, 137–150 (2019).
15. D. Naumenko, B. A. Pint and W. J. Quadackers, *Oxidation of Metals* **86**, 1–43 (2016).
16. G. Zhang, H. Zhang, J. Guo and H. Ye, *Journal of Rare Earths* **24**, 97–102 (2006).
17. K. A. Unocic and B. A. Pint, *Surface and Coatings Technology* **237**, 8–15 (2013).
18. H. Josefsson, F. Liu, J. E. Svensson, M. Halvarsson and L. G. Johansson, *Materials and Corrosion* **56**, 801–805 (2005).
19. D. W. Yun, S. M. Seo, H. W. Jeong and Y. S. Yoo, *Corrosion Science* **90**, 392–401 (2015).
20. J. G. Smeggil, A. W. Funkenbusch and N. S. Bornstein, *Metallurgical Transactions A* (1986). <https://doi.org/10.1007/BF02661258>.
21. V. V. Sidorov, V. E. Rigin, P. G. Min and Y. I. Folomeikin, *Russian Metallurgy* **2015**, 910–915 (2015).
22. J. Morscheiser, L. Thönnessen, B. Gehrman, and D. Friedrich, in *International Symposium on Liquid Metal Processing and Casting (LMPC)*. Nancy (2012). <https://doi.org/10.13140/rg.2.1.4020.8247>.

23. J. J. de Barbadillo, in *Superalloys, Metallurgy and Manufacture, Proceedings of the International Symposium 3rd, Seven Springs* (1976).
24. K. T. Chiang, G. H. Meier and R. A. Perkins, *Journal of Materials for Energy Systems* **6**, 71–86 (1984).
25. T. Gheno, G. H. Meier and B. Gleeson, *Oxidation of Metals* **84**, 185–209 (2015).
26. C. T. Rueden, J. Schindelin, M. C. Hiner, et al., *BMC Bioinformatics* **18**, 529 (2017).
27. Y. Azakli, S. Cengiz, Y. Gencer and M. Tarakci, *Corrosion Science* **143**, 249–257 (2018).
28. R. Chen, J. Guo and J. Zhou, *Journal of Materials Science and Technology* **15**, 133–136 (1999).
29. H. Okamoto, *Journal of Phase Equilibria and Diffusion* **28**, 299 (2007).
30. H. Okamoto, *Journal of Phase Equilibria and Diffusion* **36**, 292–303 (2015).
31. Y. Azakli and M. Tarakci, *Journal of Alloys and Compounds* **699**, 151–159 (2017).
32. R. Robie, B. Hemingaway, and J. Fisher, in *Thermodynamic Properties of Minerals and Related Substances at 298.15 and 1 bar (105 pascals) Pressure and at Higher Temperatures* (US Government Printing Office, Washington, 1978).
33. R. Swadźba, L. Swadźba, J. Wiedermann, M. Hetmańczyk and B. Witala, *Oxidation of Metals* **82**, 195–208 (2014).
34. P. Burtin, J. P. Brunelle, M. Pijolat and M. Soustelle, *Applied Catalysis* **34**, 225–238 (1987).
35. T. Tsuchida, R. Furuichi, T. Ishii and K. Itoh, *Thermochimica Acta* (1983). [https://doi.org/10.1016/0040-6031\(83\)85009-6](https://doi.org/10.1016/0040-6031(83)85009-6).
36. F. H. Stott, G. C. Wood and J. Stringer, *Oxidation of Metals* **44**, 113–145 (1995).
37. C. S. Giggins, B. H. Kear, F. S. Pettit and J. K. Tien, *Metallurgical Transactions* **5**, 1685–1688 (1974).
38. F. A. Golightly, F. H. Stott and G. C. Wood, *Oxidation of Metals* **10**, 163–187 (1976).
39. S. Jonas, F. Nadachowski and D. Szwagierczak, *Ceramic International* **25**, 77–84 (1999).
40. I. Kohatsu and G. W. Brindley, *Zeitschrift für Physikalische Chemie* **60**, 79–89 (1968).
41. C. Ghoroi and A. K. Suresh, *AIChE Journal* **53**, 502–513 (2007).
42. Y. Tian, X. Pan, H. Yu and G. Tu, *Journal of Alloys and Compounds* **670**, 96–104 (2016).
43. A. Kaiser, B. Sommer and E. Woermann, *Journal of the American Ceramic Society* **75**, 1463–1471 (1992).
44. S. Song, and A. Garbers-Craig, in *Advances in Molten Slags, Fluxes, and Salts: Proceedings of the 10th International Conference on Molten Slags, Fluxes and Salts 2016* (2016). https://doi.org/10.1007/978-3-319-48769-4_91.
45. M. Nath, S. Song, A. M. Garbers-Craig and Y. Li, *Ceramic International* **44**, 20391–20398 (2018).
46. D. E. Smith, T. Y. Tien and L. H. Vlack, *Journal of the American Ceramic Society* **52**, 459–460 (1969).
47. I. Kontoulis and B. C. H. Steele, *Journal of the European Ceramic Society* **9**, 459–462 (1992).
48. H. C. Graham and H. H. Davis, *Journal of the American Ceramic Society* **54**, 89–93 (1971).
49. A. Muan, *Geochimica et Cosmochimica Acta* **39**, 781–802 (1975).

Publisher's Note Springer Nature remains neutral with regard to jurisdictional claims in published maps and institutional affiliations.